Experimental investigation of water sensitivity effectson microscale mechanical behavior of shale

Wei Zhang[1,1], Dongxiao Zhang[1,1], and Junliang Zhao[1,1]

[1]Peking University

November 30, 2022

Abstract

Drilling and multi-stage hydraulic fracturing bring a large amount of water into the formation, and clay-bearing shale reservoirs interact with water, which may lead to reduction of gas production, attenuation of fracturing effects, and even wellbore instability. Because of the complex fabric of shale, a thorough understanding of changes in shale micromechanics and corresponding mechanisms when exposed to water remains unclear. In this work, representative terrestrial and marine shale samples were selected for experiments based on clay enrichment. Then, contact resonance (CR) technique was performed to characterize micromechanics of shale after exposure to water. Visual phenomena provided by environmental scanning electron microscopy (ESEM) assisted to explain the underlying mechanisms. It was found that the hydration effect lowered both the storage modulus and stiffness of samples, but with different contributions from brittle minerals and clay, as well as variations depending on bedding plane orientation. Owing to the difference in composition, terrestrial shale exhibited stronger water sensitivity and anisotropy, with a general 15%-25% decrease in modulus, while marine shale changed relatively little (-5%-15%). Moreover, microscopic observation experiments revealed that complex interaction mechanisms may have existed that produced the mechanical changes. The reduction of capillary force and the interlaminar swelling of clay particles after water adsorption weakened the strength-related behavior of shale. However, the swelling-caused confining effect or void space closure during the water imbibition process might have offset this weakening effect, and even increased mechanical properties. At mesoscale, excessive shrinkage caused the growth of micro-cracks, which significantly attenuated overall mechanical behavior.

Experimental investigation of water sensitivity effects on microscale mechanical behavior of shale

Wei Zhang[1], Dongxiao Zhang[2*], and Junliang Zhao[3]

[1]BIC-ESAT, ERE and SKLTCS, College of Engineering, Peking University, Beijing 100871, P.R. China. Email: joelzwei@pku.edu.cn

[2]School of Environmental Science and Engineering, Southern University of Science and Technology, Shenzhen 518055, P.R. China. Email: zhangdx@sustech.edu.cn

[3]BIC-ESAT, ERE and SKLTCS, College of Engineering, Peking University, Beijing 100871, P.R. China. Email: 1301111464@pku.edu.cn

*Corresponding author: Dongxiao Zhang. Email: zhangdx@sustech.edu.cn

Key Points:

- Comparison of clay composition between terrestrial and marine shale samples based on clay enrichment experiment
- Newly-developed contact resonance method to characterize the micromechanical properties of shale before and after water adsorption
- Microscale investigation of mechanisms of mechanical changes in hydration and dehydration processes

Abstract

Drilling and multi-stage hydraulic fracturing bring a large amount of water into the formation, and clay-bearing shale reservoirs interact with water, which may lead to reduction of gas production, attenuation of fracturing effects, and even wellbore instability. Because of the complex fabric of shale, a thorough understanding of changes in shale micromechanics and corresponding mechanisms when exposed to water remains unclear. In this work, representative terrestrial and marine shale samples were selected for experiments based on clay enrichment. Then, contact resonance (CR) technique was performed to characterize micromechanics of shale after exposure to water. Visual phenomena provided by environmental scanning electron microscopy (ESEM) assisted to explain the underlying mechanisms. It was found that the hydration effect lowered both the storage modulus and stiffness of samples, but with different contributions from brittle minerals and clay, as well as variations depending on bedding plane orientation. Owing to the difference in composition, terrestrial shale exhibited stronger water sensitivity and anisotropy, with a general 15%-25% decrease in modulus, while marine shale changed relatively little (-5%-15%). Moreover, microscopic observation experiments revealed that complex interaction mechanisms may have existed that produced the mechanical changes. The reduction of capillary force and the interlaminar swelling of clay particles after water adsorption weakened the strength-related behavior of shale. However, the swelling-caused confining effect or

void space closure during the water imbibition process might have offset this weakening effect, and even increased mechanical properties. At mesoscale, excessive shrinkage caused the growth of micro-cracks, which in turn significantly attenuated overall mechanical behavior.

1. Introduction

The initial water saturation of a high-quality gas shale reservoir is usually less than 45% (Boyer et al., 2006; Wang & Reed, 2009), and most of the water is in the bound state and cannot move under reservoir conditions. However, drilling and multi-stage hydraulic fracturing of horizontal wells require a large amount of water. Typically, over 11,000 m^3 of water was required per well for shale reservoirs in seven states of the U.S. from 2008 to 2014 (Chen & Carter, 2016). According to data of frac flow back volumes of fracturing fluid, 60% to 90% of the injected liquid remains in the shale formation (Penny et al., 2006). These large amounts of residual drilling fluids and fracturing fluids interact strongly with the formation due to prolonged exposure time, and cause formation damage or other significant impacts on the properties of shale reservoirs (Shaoul et al., 2011). In addition, the problem of wellbore instability resultant from swelling in clay-rich shale reservoirs when exposed to water would directly bring about substantial economic losses (Al-Awad & Smart, 1996).

Firstly, water-shale interactions directly limit the gas production rate, and the expansion of clay will alter the seepage channels to some extent and reduce the permeability of the reservoir (Civan, 1999; Santos et al., 1997). Experiments have also demonstrated that water will cause a reduction in gas diffusivity (Yuan et al., 2014) and gas transport rate in kerogen nanopores (Kadayam Viswanathan et al., 2011). Secondly, in terms of fracturing design, the hydration reaction of shale will change the mechanical properties of the reservoir, including enduring alterations in elastic mechanics and brittleness (Wang et al., 2015; Yuan et al., 2014), and stress distribution (Yew et al., 1992), which further result in permeability impairment (Meng et al., 1996). Water-based fracturing fluids can also cause some undesirable impacts on the surface of the created fractures within the shale formation, rendering damage to the fracture network (Akrad et al., 2011). Such phenomena significantly affect the fracturing and production process. Therefore, much research has been carried out on the effect of water content on the mechanical properties of shale (Hu et al., 2014; Lai et al., 2016; Meng et al., 2005; Eeckhout, 1976; Eeckhout & Peng, 1975). Moreover, wellbore-stability assurance and quantification, embedment of proppants into weakened rocks, and hydraulic fracturing aperture estimation are serious concerns induced by water-shale interactions (Han, 2003; Kumar et al., 2015). Therefore, it is of considerable significance to elucidate the interactions between shale reservoirs and water, as well as the corresponding influence mechanisms, for shale gas development.

Clay is a special and vital component in shale reservoirs, and exerts an essential impact on the petrophysical properties of shale. The expansion resultant from water-shale interactions is mainly related to clay minerals in the rocks. Experiment results on the effect of clay content on fracture conductivity after encountering water have shown that, for clay-rich shales, fracture conductivity can only return to approximately 20% of its initial state (Zhang et al., 2015). Clay minerals found in shales mostly include montmorillonite, illite, kaolinite, and chlorite. These leading composites have a significant effect on mechanical properties (Mondol et al., 2008). Indeed, due to their laminal structure, they can exert a profound impact on elastic moduli by expanding their structure as water enters the interlayers. Swelling in clays originates primarily from two mechanisms: crystalline swelling and osmotic swelling (Anderson et al., 2010). The first type of clay hydration swelling is caused by hydration of interlayer exchangeable cation, i.e., adsorption of water on the monolayer of the clay surface (Ferrage, 2005; Likos & Lu, 2006; Norrish, 1954). Crystalline swelling can be further classified as either intracrystalline or intercrystallite swelling, and the latter can occur in any type of clay, irrespective of its mineralogy (Ng & Menzies, 2007; Norrish, 1954). Osmotic swelling, on the other hand, is due to the difference in electrolyte concentration. Since cation concentration between the clay layers is greater than cation concentration in the solution, water will penetrate into the clay crystal layers and produce swelling (Gonçalvès et al., 2010).

While the microscopic composition of shale exhibits a complex fabric, mainly including organic matter, clay and granular minerals, such as quartz, feldspar and pyrite (Bai et al., 2013), the complex structure of shale with mineral inclusions makes the actual swelling much more complicated than pure clay minerals (Ghanbari & Dehghanpour, 2015). Overall, the influence of different inclusions on the mechanical properties of shale is poorly understood. Acoustic logs with enhanced resolutions are widely utilized for quantifying mechanical properties of formations at a relatively large scale (Huang et al., 2015; Huang & Torres-Verdín, 2016). Ultrasonic velocities are also used to investigate dynamic mechanical properties of rock, and it was found that, as water content increases, Young's modulus and shear modulus decrease simultaneously (Lai et al., 2016). However, the abovementioned experiments only provide bulk properties averaged from both intact and weakened parts of the rock, and it is difficult to perform direct macro-mechanical measurements on the micro particles. This also indicates that micromechanical tests can better assist us to explain the micro-mechanisms of water-shale interactions.

Nano-indentation technology obtains modulus values from forces and displacements acting on tiny samples (Abousleiman et al., 2009), and is a measurement technology that does not damage the samples (Oliver & Pharr, 1992). Experiments have been performed to well characterize the mechanical properties of shale with varied compositions at a multiplicity of scales (Zhao et al., 2019). Furthermore, this technology was used to investigate the change of Young's modulus in fracturing fluid environmental applications (Akrad et al., 2011; Wu et al., 2020). However, due to the influence of resolution, the test results still cannot analyze different tiny particles. The PeakForce QNM™ technique in atomic force microscopy (AFM) has also recently been developed to map the mechanical properties of shale. A serious problem with such technique, however, is that its maximal range is below the Young's modulus of pyrite (Eliyahu et al., 2015), which is reported to be over 250 GPa (Kumar et al., 2012; Mavko et al., 2009). Therefore, we need to discover a more effective way to characterize micromechanics before and after the interaction with water by considering additional influencing factors. Research also shows that uncertainty of test results can also arise from bedding plane orientation, which can significantly affect anisotropic behavior (Alqahtani et al., 2013; Wong et al., 2008). However, in previous works, the influence of anisotropy during exposure to water has rarely been investigated.

Consequently, in this work, we investigate the effects of water-shale interactions for different bedding plane orientations and varying mineralogy on elastic mechanical properties. We carried out XRD tests, clay enrichment experiments to classify mineralogy, and applied a new method - contact resonance (CR) - to characterize mechanical properties, including stiffness, elastic, and viscoelastic properties. Similarly, we attempted to provide visual information by conducting microscopic observations on the behaviors of water-rock reactions in shale to better understand the underlying mechanisms.

2. Materials and Theory

2.1 Sample information and clay enrichment analysis

The samples used in this work are of terrestrial shale from the Yanchang formation in the Ordos Basin, China, with different strata ages, and of marine shale from the Longmaxi formation in the Sichuan Basin, China, which are all considered to be typical oil and gas production fields. Whole-rock X-ray diffraction (XRD) analysis was carried out to obtain mineral compositions (Terra XRD Analyzer, Olympus) of the two series of samples (Table 1). The results showed that the samples mainly consisted of pyrite, quartz, feldspar, carbonate and clay minerals, together comprising over 80%. Moreover, significant differences existed in constituent contents under different sedimentary environments. Firstly, marine shale consisted of relatively more carbonates than terrestrial shale. Marine shale also had a high content of brittle minerals (quartz-feldspar-pyrite) with 30%-50% quartz, while the content of clay minerals only reached 20%-30%. In comparison, the content of brittle minerals of terrestrial shale was relatively low, but with a very high content of clay minerals (up to 70%), which can be regarded as the matrix of terrestrial shale. Since clay plays a vital role in water sensitivity, clay enrichment experiments were carried out with the Chinese national standards "SYT 5163-2010" (Zeng et al., 2010), that yielded a semi-quantitative study of each type of clay mineral.

The shale core samples were first ground to powders of less than 100 mesh using a grinder. Then, approximately 50 g powders were placed into beakers, and the organic matter and the carbonate were, respectively, removed by adding hydrogen peroxide and EDTA under a water bath heated at 70 °C. The clay minerals were suspended using sodium hexametaphosphate as a suspending agent and separated from other impurities following Stokes' law. The suspension liquid was then extracted for centrifugation, and clay particles of less than 2 μm were collected and made as test samples. The XRD of clay was measured by a ZJ207 Bruker D8 (24℃, 49% RH) in the natural state. The samples were then saturated with ethylene glycol vapor for 12 h at 60 °C, and the same XRD testing process was repeated. Similarly, high-temperature heated state (450 °C, >2.5 h) results were also obtained (Figure 1). The relative content of clay minerals in shale samples could be derived based on its characteristic peak intensity (Table 2). In addition, the proportion of smectite in the illite-smectite mixed-layer was estimated based on the method derived from the following equation (Reynolds, 1980):

$$I/(I/S) = \frac{I_{1.0nm}(\mathrm{EG})}{I_{1.0nm}(\mathrm{H}) - I_{1.0nm}(\mathrm{EG})} \tag{1}$$

where $I/(I/S)$ is the content ratio of illite to illite-smectite mixed-layer in the sample; and $I_{1.0\mathrm{nm}}$ (EG) and $I_{1.0\mathrm{nm}}$ (H) are diffraction peak intensity of 1.0 nm on the ethylene glycol-saturated sample and 450℃-550℃ heated sample, respectively.

The clay enrichment results revealed that the representative clay minerals of different series of samples were entirely different. The composition of clay minerals in marine shale was relatively simple, mainly dominated by illite and illite/smectite mixed-layers. The terrestrial shale also contained a certain proportion of kaolinite and chlorite. Moreover, kaolinite accounted for the major part of the Permian terrestrial samples in this study. There were no pure smectite components found in the samples chosen in this work, perhaps due to the limitation of samples.

2.2 Mechanical characterization method - Contact resonance (CR)

Contact resonance (CR) mapping is a recent AFM resonance-based mode to measure the elastic moduli or other mechanical properties of samples by detecting resonance frequencies of the probe under contact of the sample surface. The technique has already been used to characterize the viscoelastic properties of a thin PMMA film (Yuya et al., 2008), contact stiffness of nanotubes (Stan et al., 2008), elastic properties of DNA molecules (Gannepalli et al., 2011), and elastic stiffness of titanium alloys (Phani et al., 2016). Yang (2017) employed this method for the first time to characterize the mechanical stiffness of organic matters in shale, but did not further measure the storage moduli and viscoelastic properties of other main constituents in shale.

In CR test mode, the probe performs a point-by-point force curve measurement on the surface of the sample. During each force curve period, the amount of cantilever bending is maintained constant after the probe contacts the sample, and the controller emits a series of signals with different frequencies and fixed amplitudes to the actuator, causing the sample and probe to vibrate (Figure 2a). For a rigid, thin and long beam, its deflection could be described using the Euler-Bernoulli formula:

$$EI\frac{\partial^4 y}{\partial x^4} = -\rho A\frac{\partial^2 y}{\partial t^2} + q \tag{2}$$

where E is Young's modulus of the cantilever; I is the area moment of inertia; ρ is its mass density; A is the area of its cross-section; y is deflection at time t and location x;

and q is distributed load. When the beam is oscillating in the air without external loading, then q equals fluid resistance (Weaver Jr et al., 1990):

$$EI\frac{\partial^4 y}{\partial x^4} = -\rho A\frac{\partial^2 y}{\partial t^2} - \eta\rho A\frac{\partial y}{\partial t} \tag{3}$$

where η is a constant expressing dissipation in air.

The general solution of the differential equation of motion can be expressed as follows:

$$y(x,t) = (A_1 e^{\alpha x} + A_2 e^{-\alpha x} + A_3 e^{i\alpha x} + A_4 e^{-i\alpha x})e^{i2\pi f_n t} \tag{4}$$

where f_n is natural frequency; α is wave number; and A_1, A_2, A_3, and A_4 are constants determined by boundary conditions. By substituting equation (4) in equation (3), we can obtain the dispersion relation:

$$\alpha = \pm\sqrt[4]{\frac{\rho A}{EI}[(2\pi f)^2 \mp i\eta 2\pi f_n)]}\,. \tag{5}$$

In the absence of fluid resistance, the equation simplifies to:

$$f_n = \frac{\alpha^2}{2\pi}\sqrt{\frac{EI}{\rho A}}\,. \tag{6}$$

The solutions of the characteristic equation of surface-coupled beam are determined for different boundary conditions (Rabe, 2006).

By detecting the amplitude and phase of the probe vibration at different frequencies, the resonance spectra are measured, and quality factors (Q) and CR frequencies in each pixel of the tested surface can be obtained (Figure 2b) (Killgore et al., 2011; Rabe, 2006; Yuya et al., 2008, 2011). According to the relationship between CR frequency and contact stiffness, the equivalent constant of each point on the surface can be derived (Rabe, 2006). Combined with the Hertzian model assumption, which describes the contact between two elastic bodies (Johnson, 1987), the relationship between reduced Young's modulus E^* and contact stiffness k^* is:

$$E^* = \sqrt{\frac{k^{*3}}{6RF}} \tag{7}$$

where F is the normal force; and R is the tip radius based on the spherical assumption. E^* is also given by:

$$\frac{1}{E^*} = \frac{\left(1-\nu_S{}^2\right)}{E_S} + \frac{\left(1-\nu_T{}^2\right)}{E_T} \tag{8}$$

where E_s, E_T, and υ_s, υ_T represent Young's modulus and Poisson's ratio of the sample surface and the tip, respectively. Finally, the elastic modulus and viscoelastic property (quality factor, Q) distribution of the sample can be obtained. The Poisson ratio used in this work was assumed to be 0.3.

3. Experimental Method

3.1 Test procedure

Samples Y13, Y21 and YC2 were chosen to represent terrestrial shale, while YS109 and YS111 stand for marine shale. In order to investigate the influence of anisotropy, each type of sample was cut into two small cubes of 7x7x4 mm, with the larger faces (test faces) either parallel or perpendicular to the bedding planes. Then, the test faces were milled using argon ion milling (Leica EM TIC 3X, accelerating voltage 5 kV) for an extremely smooth surface with roughness below 100 nm of a 25x25 μm test area. Because this work aimed to examine the water sensitivity of shale rocks, the sample was placed in a vacuum drying-oven for dehydration firstly (60°C, drying for 24 h, enabling removal of most inter-water of clay particles, but retaining rapid rehydration capacity). Mechanical tests were then carried out at preselected areas of the sample. After that, the sample was immersed in deionized water at 25°C for 10 d. Subsequently, all of the above tests were repeated after the water spontaneous imbibition process.

Scanning electron microscopy (SEM) was utilized to observe the sample surface with an accelerating voltage of 15 kV in a low vacuum condition (Quattro S ESEM, Thermal Fisher). Moreover, different constituents and chemical element maps were identified and imaged using an energy dispersive spectrometer (EDS) operated at 15 kV (EDS, MAX100, Oxford). Topography scanning was then operated to identify the chosen test regions in the atomic force microscopy (AFM, DimensionXR, Bruker). The reflectivity and convex morphology of the pyrite grains in the shale assisted to rapidly locate the scanning area in the AFM optical microscope. By obtaining topographic and peak force error images, and comparing them with SEM images, the final position to perform mechanical characterization was determined. With the high degree of freedom of the probe in contact resonance mode and the nanometer radius of the tip, extremely high-resolution test images could be achieved. Therefore, this method provided excellent statistical characterization for complex samples with high heterogeneity and large surface topography fluctuation. Here, we used a resolution of 388x388 of 25x25 μm areas for testing.

Due to the limited range of moduli that can be measured for a given spring constant probe, for shale samples with complex compositions that included both hard minerals (such as pyrite, quartz, and feldspar) and soft minerals (such as clay and organic matter), the probe needed to be sufficiently stiff to compress the test sample, but simultaneously not too stiff to lose cantilever bending sensitivity. For this reason, selecting a probe with a suitable spring constant was essential for accurate measurement in CR mode. In this work, tips coated with a conductive diamond were chosen (DDLTESP-V2; Bruker; spring constant 65 N/m). After each laser alignment, the deflection sensitivity of the probe was determined by pressing the probe on a sapphire sample (E = 345 N / m) to obtain force curves. The spring constant was calibrated by the Sader method (Sader et al., 1995) with the factors, free air natural frequency v_0 and free air quality factor Q, determined by the thermal tune method (Belikov et al., 2014). An effective CR tip radius was verified by scanning a standard silicon sample (165 GPa).

In order to satisfy the Hertzian model hypothesis and reduce the error of model fitting as much as possible at the same time, the surface deformation of the sample was controlled in the range of 2-20 nm and the deformations of the organic matter and other different minerals were ensured to be as close as possible by applying a constant peak force set point. This step was also taken to ensure that normalized contact stiffness was controlled at approximately 10-100 to increase sensitivity. Furthermore, the scan rate and ramp rate were set to 0.5 Hz and 5 Hz, respectively, and the trig threshold and modulate amplitude were set to guarantee that the resonance signal was significant and stable. However, due to the limitation of the frequency sweep range of the software, this test could only achieve the first eigenmode, and the ratio between lateral and normal contact stiffness was assumed to be a constant (Rabe, 2006). Since the probe was not removed from the scanner before and after the comparison experiment, the laser position was not changed to ensure the same measurement parameters. A test was performed with standard samples before and after the experiment to be certain that the probe tip did not show excessive wear or contamination and the effective parameter tip radius did not change. When necessary, after several scans, tapping mode was used to clean the tip on a roughness Ti sample.

3.2 Microscopic observations of water-shale interactions

To better understand water-shale interactions, and to elucidate the mechanisms of variations in micromechanics, we utilized environmental scanning electron microscopy (ESEM) to observe the reaction process (Quattro S ESEM, Thermal Fisher). Compared with traditional SEM, ESEM possesses the advantage that it can place the sample in a specific atmospheric environment, such as water vapor, to observe the changes. In order to effectively find the clay particles in the natural state, we used a natural block of rock and a polished sample to experiment separately. Usually, according to the three-phase curve of water at room temperature, the pressure of the electron microscope chamber needs to reach at least 3000 Pa to allow moisture to precipitate on the sample surface. However, the ion beam will be severely scattered by the air in such pressure, and image resolution is greatly affected. In this work, a cold stage auxiliary device was installed at the bottom of the sample to decrease the temperature of the sample surface and its surrounding atmosphere (Figure 3a), thereby reducing the saturated vapor pressure needed for water precipitation.

Here, we defined the relative humidity of the environment as the ratio of the vapor pressure of water in the chamber to the saturated vapor pressure of water at the corresponding temperature. In the experiment, the cold stage was set to 2°C (at this time, the corresponding saturated vapor pressure was 700 Pa) (Figure 3b), and thus the purpose of controlling the humidity of the environment could be achieved indirectly by adjusting the water vapor pressure in the chamber. In this process, it was necessary to control the upper limit of humidity; otherwise, the excessive precipitation of water on the surface would quickly flood the observation area. In order to observe the dynamic process of hydration and determine whether the process was reversible, the target humidity was set at several levels, which were 0%, 60%, and 80%. Finally, the vacuum was re-evacuated to make the humidity reach 0% and remove water.

4. Results and Discussion

4.1 Mechanical characterization results of shale samples

According to the SEM images and EDS elemental maps of one test region of sample Y21a (test face parallel to the bedding plane) (Figure 4), different constituents could be identified. Among them, the flocculent materials were clay minerals, the round-shaped minerals with surfaces higher and brighter than other micro-components were pyrite, the black agglomerates were organic matters, and other components were mostly quartz and feldspar. No obvious carbonate particles were detected in the areas selected in this study. In each scan, we could obtain the topography images, resonance frequencies, and storage moduli of different micro-compositions calculated according to the formula. It was not difficult to find that the resonance frequencies and mechanical properties of different micro-components in shale were very different (Figure 5).

For the test region of sample Y21b (test face perpendicular to the bedding plane), results could be divided into four different constituents, according to contact frequency and storage modulus mapping. With the assistance of the high-resolution features of the AFM results, we could extract the images of different minerals according to the threshold segmentation method (Al-Amri et al., 2010) of the electron images (Figure 6). In addition, by deriving probability density functions and Gaussian mixture models of resonance frequency and storage modulus results, respectively, we could obtain the mechanical estimations of different constituents (Figure 7): (1) the pyrite mineral, which behaved as the stiffest constituent, with its storage modulus exceeding 90 GPa, and the mean value of resonance frequency being approximately 989±16 kHz; (2) quartz and feldspar grains, with an average of 69 GPa (928±23 kHz), which was similar to the typically reported ranges for quartz (77- 96 GPa (Mavko et al., 2009)), and the difference in test results may have originated from crystal orientation (Timms et al., 2010); (3) the clay minerals (mainly composed of illite, illite-smectite mixed-layer, and Fe-chlorite in this work), with a mean value of approximately 37 GPa (886±28 kHz); and (4) the organic matter served as the softest constituent, at only approximately 15 GPa (811±48 kHz) in this test area. There were several different sets of peaks in the resonance frequencies of the tested organic matter, which might correspond to bituminous material or kerogen, or kerogen with different maturity (Kumar, 2012). Table 3 presents a comparison with previously reported moduli of different constituents in shale. Measured CR moduli showed good agreement with values reported in these literatures.

We can observe that the mean value of the storage modulus of clay minerals with test regions perpendicular to the bedding plane (37.6 GPa of Y21b) was higher than that of regions parallel to the bedding plane (23.6 GPa of Y21a). Such a phenomenon was also confirmed by other studies (Sone & Zoback, 2013; Wu & Tan, 2010), in which dynamic storage modulus was measured with the ultrasonic method. Furthermore, in the organic constituent, some invalid data existed. Compared with the SEM images, such invalid data may suggest nanopores or voids, and at these points, it was difficult for the tip to establish good contact and cause resonance. In addition, in tests on the surface of some hard minerals, abnormally low values would be generated. Combined with the EDS spectrum, we can infer that this may be due to some organic matter coating or contamination on the surface of these mineral particles. These adhesions may be caused during the sample preparation or polishing process.

4.2 Mechanical property variations due to water imbibition

With the assistance of contact resonance mode, we could characterize and compare the storage modulus, stiffness, and other viscoelastic properties of the test areas before and after water adsorption. The test region Y13a (Figure 8) was taken from the terrestrial shale samples with the test face parallel to the bedding plane. The surface was distributed with brittle minerals, such as pyrite, quartz and feldspar, as well as clay particles with different water sensitivity, such as Fe-chlorite and illite. From the perspective of storage modulus, the mechanical properties changed significantly after water adsorption, with an overall downward trend. The specific statistics of different minerals revealed a massive difference, and the water sensitivity of the clay part was significant. The mechanics of chlorite were weakened by nearly 40%, and illite was nearly 30%. In comparison, the change of the feldspar quartz part was relatively weak, but still with a 20% reduction. This might be related to the existence of certain water-sensitive minerals below the surface, and the changes in the properties of these minerals would also exert a certain impact on the test results of the test surface. The mechanical properties of pyrite were nearly unchanged, and the variations were within measurement errors. The stiffness variation results showed similar trends, which met our expectations. Regarding viscoelastic properties, the process of water imbibition made the quality factors of the clay minerals rise significantly.

In order to obtain more statistical results, we selected four samples of the terrestrial and marine shales with faces parallel and perpendicular to bedding planes for testing. In addition, 10 test areas were selected for each sample to obtain an average of 4-5 uncontaminated and valid regions after immersion in water, and each area could produce more than 350x350 valid data points (Figure 9). It can be seen from the experiment results that (Figure 10) because the terrestrial shale was bearing more clay minerals than the marine shale, its water-sensitive properties were also stronger and more anisotropic. The terrestrial shale samples parallel to the bedding plane had an average of 30% storage modulus decrease, and the perpendicular bedding direction could also reach nearly a 20% decrease. Such results and differences can be explained as that the shale soaked in deionized water had a swelling strain of 0.25% in the direction perpendicular to the bedding and 0.15% in the direction parallel to the bedding (Yuan et al., 2014). Marine shale hardly exhibited strong water-sensitive properties, with a change of only approximately 10%, which was consistent with previous work (Wu et al., 2020). However, in some test areas, an increase in modulus could be seen. The reason for such a phenomenon will be discussed in the subsequent mechanisms part based on microscale observation experiment results.

4.3 Microscopic mechanisms analysis

Firstly, in an area of 40x30 μm scale, as shown in Figure 11, one can see that a large number of clustered clay particles developed in this natural depression. Due to its poor resistivity, under the electron beam, it was easy to accumulate charges on the surface and generate a discharge phenomenon. Most of the grayish-black particles were brittle minerals, such as quartz and feldspar. At a relative humidity of 0%, the clay particles were relatively dispersed, and as the humidity gradually increased to 60%, water molecules began to adhere to the surface of the particles, and the discharge phenomenon was further enhanced. The clay particles began to adsorb water and expanded in volume with clusters adhering to each other. When the humidity was further increased to 80%, the hydration phenomenon was further aggravated with a large area covered with water. Compared with clay particles, quartz and feldspar exhibited weaker hydrophilicity. Subsequently, the water was removed 3 h later as we evacuated to regain a vacuum state.

In order to compare the hydrophilic properties of different minerals, we simultaneously selected several different observation areas for a fully synchronized humidity saturation process, as shown in Figure 12. When increasing the relative humidity from 0% to 80%, the substances showed significant differences in hydrophilicity. The clay hydration phenomenon in Figure 12a exceeded the quartz or feldspar minerals in Figures 12b and Figures 12c.

Next, the observation area was narrowed down to 3x2 μm to observe the hydration process of a single clay particle at a smaller scale. As shown in Figure 13, we repositioned a clay particle of approximately 500 nm for observation, and set the same humidity change cycle as previously. It can be seen that when the humidity reached 60%, a bridge of water film appeared between the clay particles, marking the water film radius at this time as R_1. Limited by the resolution of the instrument here, we could not observe internal swelling of the clay particles, but this phenomenon has been confirmed by X-rays (Norrish, 1954). When the humidity continued to increase to 80%, the water film further expanded, and the radius of curvature increased to R_2. Finally, the vacuum was re-evacuated to reduce the humidity to 20%, and the water film shrank with the radius of curvature decreased to R_3.

Finally, we re-scaled the observation area to mesoscale, and recorded the changes in morphology after hydration and dehydration. In order to better observe the developed flocculated bedding of clay, we chose a polished sample perpendicular to the bedding plane. In Figure 14, when the humidity increased from 0% to 80%, the clay layer expanded visibly. However, this expansion might close the void space between the clay layers and some well-developed crack channels to a certain extent, which would further result in squeeze and compaction. Figure 15 presents an opposite humidity change process. The figure shows that, after water adsorption and expansion, with the decrease of humidity, some new micro-cracks were generated, or areas where cracks already existed continued to derive and expand (Figure 15a and Figure 15b), and these developed cracks would greatly attenuate mechanical behavior.

To summarize the above phenomena, the shale hydration and dehydration process should be discussed from nanoscale to mesoscale to analyze the complex mechanisms of variations in shale micromechanics. At nanoscale, water films formed between the clay particles after moving from an arid environment to a humid environment. Here, the water film caused attraction forces to form between the clay particles, and can be described by using the following formulas (Gröger et al., 2003; Mason & Clark, 1965):

$$F = 2\pi b\sigma + \pi b^2 P_c \tag{9}$$

with

$$P_c = \frac{2\sigma\cos\theta}{R} \tag{10}$$

where σ is the surface tension; b is the radius of the liquid bridge; and P_c is the capillary pressure.

As the ambient humidity further rose, the radius of curvature of the water film began to increase. In turn, the capillary force began to decrease, and the attraction force between the particles weakened. However, when the moisture content started to reduce, the radius of curvature decreased, which increased the attractive force and would reinforce the particles. At this scale, the dynamic water adsorption process reduced the compactness of the clay particles, while dehydration would shrink the interlayer distance and increase particle intensity and compactness.

Regarding the microscale phenomena, it is clearer to observe the clay swelling in the presence of water. The hydration might partially separate clay minerals from each other or serve as a lubricant, thereby greatly diminishing the strength of the clay. However, because clay often displays a disorderly dispersed arrangement, the swelling between its layers would also compress or close the interlayer space and exert a confining effect on the surrounding minerals. Such effect would thereby increase the confining pressure of the minerals, and to some extent, increase the modulus values of the measured particles (Mogi, 2006; Ong et al., 2015; Wong et al., 2008), as shown in Figure 15c. Moreover, in the process of losing moisture, the continuously increasing interparticle attraction force at nanoscale would result in shrinkage between clay layers and close the interlayer space at microscale. However, from a more direct perspective, according to the Griffith criterion (Eeckhout, 1976):

$$\sigma_t = \left(\frac{2E\gamma}{\pi c_0}\right)^{\frac{1}{2}} \tag{11}$$

where σ_t is the tensile stress required for crack growth; E is storage modulus; γ is surface energy; and c_0 is half of the initial crack length.

The dynamic water adsorption process will weaken the surface energy, i.e., reduce the tensile stress necessary for crack formation and expansion. From the above discussion, shrinkage generated during the dynamic dehydration process will induce cracks to develop. From this perspective, the severe dynamic dehydration process will lead to a decline of mechanical properties as cracks grow (Nur & Simmons, 1969) at mesoscale.

5. Conclusion

In this work, the contact resonance (CR) method was performed to characterize the micromechanical properties of shale. Variations of mechanical properties of different minerals in different bedding plane orientations after water-shale interactions, and the corresponding mechanisms, were investigated and discussed. The following conclusions can be drawn:

(1) The clay enrichment experiment results indicated that the compositions of the terrestrial and marine shales were significantly different. The terrestrial samples investigated in this work contained more clay minerals, and their clay composition types were much more complex.

(2) The contact resonance (CR) technique could well map the mechanical properties of shales with nanoscale resolution. It could achieve similar results, but with higher resolution, compared to previous work, and thus we conclude that the CR method provides an effective means to characterize brittle minerals (especially pyrite) and tiny clay particles within shale at the same time. By combining image segmentation to perform mechanical tests on different minerals, we found that the mechanical properties of different minerals varied greatly, and posed strong anisotropy due to the laminal structure of the clay layers.

(3) In general, strength-related mechanical properties, such as storage modulus and stiffness, of shale would decrease after shale interacts with water. Among minerals, clay exhibited the most active water-sensitive properties (16% decrease in storage modulus, on average, of samples used in this work), and its viscoelastic properties would be strengthened post-hydration. At the same time, lesser changes of mechanical behavior were expected for brittle minerals (quartz, feldspar, and pyrite). In comparison, the decrease in modulus values tended to be higher (15%-25% reduction) for terrestrial shale due to its clay-rich feature, while the properties of marine shale changed relatively little (-5%-15%). In addition, anisotropy of water sensitivity was found when considering bedding plane orientations, and such difference was also mainly attributable to the contribution of the clay laminal structure, especially for illite-smectite mixed-layer and chlorite content.

(4) The mechanisms of mechanical variations in water might be complex and competitive. Humidity saturation experiments revealed significant differences in the hydrophilic properties of shale micro-components. Moreover, humidity changes caused

hydration and dehydration, which could lead to microstructural changes, and produce complex influences on mechanical properties. Specifically, the increase in humidity would decrease the capillary force, and thus weakened cohesion between particles at nanoscale. In turn, the loss of moisture content increased particle compactness and density. Concerning microscale, although the interlaminar swelling of clay has been proven to reduce the strength of the clay, the confining effect (increase of confining pressure) and void space closure brought by anisotropic swelling might have offset this weakening effect, and even strengthened rock in some areas instead. From this point of view, the effect of swelling might be similar to the mechanical influence of shrinkage during dehydration, which would also improve the mechanical performance of the rocks. However, at mesoscale, losing water caused excessive shrinkage, which might stimulate and promote the growth of the micro-cracks, and in turn attenuated the overall mechanical behavior of clay-bearing shale.

Acknowledgements

This work is partially funded by the National Natural Science Foundation of China (Grant No. 51520105005 and U1663208), and the National Science and Technology Major Project of China (Grant No. 2017ZX05009-005 and 2017ZX05049-003). The data used in this paper are available through this link (http://dx.doi.org/10.17632/5zwbdhy94t.1).

References

Abousleiman, Y., Tran, M. H., Hoang, S., Ortega, A., & Ulm, F.-J. (2009). *Geomechanics field characterization of the two prolific US Mid-West gas plays with advanced wire-line logging tools*. Paper presented at SPE Annual Technical Conference and Exhibition, New Orleans, Louisiana, USA. https://doi.org/10.2118/124428-MS

Akrad, O. M., Miskimins, J. L., & Prasad, M. (2011). *The Effects of Fracturing Fluids on Shale Rock Mechanical Properties and Proppant Embedment*. Paper presented at SPE Annual Technical Conference and Exhibition, Denver, Colorado, USA. https://doi.org/10.2118/146658-MS

Al-Amri, S. S., Kalyankar, N. V., & S.D., K. (2010). Image segmentation by using threshold techniques. *ArXiv Preprint ArXiv:1005.4020*.

Al-Awad, M. N., & Smart, B. G. D. (1996). Characterization of shale-drilling fluid interaction mechanisms related to wellbore instability. *Journal of King Saud University-Engineering Sciences*, *8*(2), 187–214.

Alqahtani, A. A., Mokhtari, M., Tutuncu, A. N., & Sonnenberg, S. (2013). *Effect of mineralogy and petrophysical characteristics on acoustic and mechanical properties of organic rich shale*. Paper presented at Unconventional Resources Technology Conference, Denver, Colorado, USA. https://doi.org/10.1190/urtec2013-045

Anderson, R., Ratcliffe, I., Greenwell, H., Williams, P., Cliffe, S., & Coveney, P. (2010). Clay swelling—A challenge in the oilfield. *Earth-Science Reviews*, *98*(3–4), 201–216.

Bai, B., Elgmati, M., Zhang, H., & Wei, M. (2013). Rock characterization of Fayetteville shale gas plays. *Fuel*, *105*, 645–652.

Belikov, S., Alexander, J., Wall, C., Yermolenko, I., Magonov, S., & Malovichko, I. (2014). Thermal tune method for AFM oscillatory resonant imaging in air and liquid. *2014 American Control Conference*, 1009–1014. https://doi.org/10.1109/ACC.2014.6859224

Boyer, C., Kieschnick, J., Suarez-Rivera, R., Lewis, R. E., & Waters, G. (2006). Producing gas from its source. *Oilfield Review*, *18*(3), 36–49.

Chen, H., & Carter, K. E. (2016). Water usage for natural gas production through hydraulic fracturing in the United States from 2008 to 2014. *Journal of Environmental Management*, *170*, 152–159. https://doi.org/10.1016/j.jenvman.2016.01.023

Civan, F. (1999). *Interpretation and correlations of clay swelling measurements*. Paper presented at SPE mid-continent operations symposium, Oklahoma City, Oklahoma, USA. https://doi.org/10.2118/52134-MS

Eeckhout, E. M. V. (1976). The mechanisms of strength reduction due to moisture in coal mine shales. *International Journal of Rock Mechanics and Mining Sciences &*

Geomechanics Abstracts, *13*(2), 61–67. https://doi.org/10.1016/0148-9062(76)90705-1

Eeckhout, E. M. V., & Peng, S. S. (1975). The effect of humidity on the compliances of coal mine shales. *International Journal of Rock Mechanics and Mining Sciences & Geomechanics Abstracts*, *12*(11), 335–340. https://doi.org/10.1016/0148-9062(75)90166-7

Eliyahu, M., Emmanuel, S., Day-Stirrat, R. J., & Macaulay, C. I. (2015). Mechanical properties of organic matter in shales mapped at the nanometer scale. *Marine and Petroleum Geology*, *59*, 294–304. https://doi.org/10.1016/j.marpetgeo.2014.09.007

Ferrage, E. (2005). Investigation of smectite hydration properties by modeling experimental X-ray diffraction patterns: Part I. Montmorillonite hydration properties. *American Mineralogist*, *90*(8–9), 1358–1374. https://doi.org/10.2138/am.2005.1776

Gannepalli, A., Yablon, D., Tsou, A., & Proksch, R. (2011). Mapping nanoscale elasticity and dissipation using dual frequency contact resonance AFM. *Nanotechnology*, *22*(35), 355705. https://doi.org/10.1029/2009WR008090

Ghanbari, E., & Dehghanpour, H. (2015). Impact of rock fabric on water imbibition and salt diffusion in gas shales. *International Journal of Coal Geology*, *138*, 55–67. https://doi.org/10.1016/j.coal.2014.11.003

Gonçalvès, J., Rousseau-Gueutin, P., De Marsily, G., Cosenza, P., & Violette, S. (2010). What is the significance of pore pressure in a saturated shale layer? *Water Resources Research*, *46*(4). https://doi.org/10.1029/2009WR008090

Goodarzi, M., Rouainia, M., Aplin, A., Cubillas, P., & de Block, M. (2017). Predicting the elastic response of organic-rich shale using nanoscale measurements and homogenisation methods. *Geophysical Prospecting*, *65*(6), 1597–1614.

Gröger, T., Tüzün, U., & Heyes, D. M. (2003). Modelling and measuring of cohesion in wet granular materials. *Powder Technology*, *133*(1–3), 203–215.

Han, G. (2003). *Rock stability under different fluid flow conditions* [Doctoral dissertation]. University of Waterloo, Ontario, Canada.

Hu, R., Liu, H.-H., Chen, Y., Zhou, C., & Gallipoli, D. (2014). A constitutive model for unsaturated soils with consideration of inter-particle bonding. *Computers and Geotechnics*, *59*, 127–144.

Huang, S., Matuszyk, P. J., & Torres-Verdín, C. (2015). Spatial sensitivity functions for rapid numerical simulation of borehole sonic measurements in vertical wells. *Geophysics*, *80*(5), D459–D480.

Huang, S., & Torres-Verdín, C. (2016). Inversion-based interpretation of borehole sonic measurements using semianalytical spatial sensitivity functions. *Geophysics*, *81*(2), D111–D124.

Johnson, K. L. (1987). *Contact mechanics*. Cambridge, England: Cambridge University Press.

Kadayam Viswanathan, R. K., Cao Minh, C., Zielinski, L., Vissapragada, B., Akkurt, R., Song, Y. Q., et al. (2011). *Characterization of gas dynamics in kerogen nanopores by NMR*. Paper presented at SPE Annual Technical Conference and Exhibition, Denver, Colorado, USA. https://doi. org/10.2118/147198-MS

Killgore, J. P., Yablon, D., Tsou, A., Gannepalli, A., Yuya, P., Turner, J. A., Proksch, R., & Hurley, D. (2011). Viscoelastic property mapping with contact resonance force microscopy. *Langmuir*, *27*(23), 13983–13987.

Kumar, H., Elsworth, D., Liu, J., Pone, D., & Mathews, J. P. (2015). Permeability evolution of propped artificial fractures in coal on injection of CO2. *Journal of Petroleum Science and Engineering*, *133*, 695–704.

Kumar, V. (2012). *Geomechanical characterization of shale using nano-indentation* [Doctoral dissertation]. University of Oklahoma Norman, OK, USA.

Kumar, V., Sondergeld, C. H., & Rai, C. S. (2012). *Nano to macro mechanical characterization of shale*. Paper presented at SPE Annual Technical Conference and Exhibition, San Antonio, Texas, USA. https://doi.org/10.2118/159804-MS

Lai, B., Li, H., Zhang, J., Jacobi, D., & Georgi, D. (2016). Water-Content Effects on Dynamic Elastic Properties of Organic-Rich Shale. *SPE Journal*, *21*(02), 635–647. https://doi.org/10.2118/175040-PA

Likos, W. J., & Lu, N. (2006). Pore-scale analysis of bulk volume change from crystalline interlayer swelling in Na^{+}-and Ca^{2+}-smectite. *Clays and Clay Minerals*, *54*(4), 515–528.

Mason, G., & Clark, W. (1965). Liquid bridges between spheres. *Chemical Engineering Science*, *20*(10), 859–866.

Mavko, G., Mukerji, T., & Dvorkin, J. (2009). *The rock physics handbook*. Cambridge, England: Cambridge University Press.

Meng, Y., Jiao, D., & Wu, S. (1996). *Affection of shale hydration for stress sensitive gas reservoir production*. Paper presented at SPE Gas Technology Symposium, Calgary, Alberta, Canada. https://doi.org/10.2118/35602-MS

Meng, Z., Yi, W., & Tiedemann, J. (2005). *Analysis of Mechanical Properties of Sedimentary Rocks of Coal Measures and Their Influencing Factors*. Paper presented at 40th US Symposium on Rock Mechanics (USRMS), Anchorage, Alaska, USA.

Mogi, K. (2006). *Experimental rock mechanics*. Boca Raton, FL: CRC Press.

Mondol, N. H., Jahren, J., Bjørlykke, K., & Brevik, I. (2008). Elastic properties of clay minerals. *The Leading Edge*, *27*(6), 758–770.

Ng, C. W., & Menzies, B. K. (2007). *Unsaturated soil mechanics and engineering*. Oxon, England: Taylor & Francis.

Norrish, K. (1954). The swelling of montmorillonite. *Discussions of the Faraday Society*, *18*, 120–134.

Nur, A., & Simmons, G. (1969). Stress-induced velocity anisotropy in rock: An experimental study. *Journal of Geophysical Research*, *74*(27), 6667–6674.

Oliver, W. C., & Pharr, G. M. (1992). An improved technique for determining hardness and elastic modulus using load and displacement sensing indentation experiments. *Journal of Materials Research*, *7*(6), 1564–1583.

Ong, O., Schmitt, D., & Kofman, R. (2015). Seismic anisotropy and elastic properties of a VTI medium. *3rd International Workshop on Rock Physics, Perth, Australia*, 13–17.

Penny, G. S., Dobkins, T. A., & Pursley, J. T. (2006). *Field study of completion fluids to enhance gas production in the Barnett Shale*. Paper presented at SPE Gas Technology Symposium, Calgary, Alberta, Canada. https://doi.org/10.2118/100434-MS

Phani, M. K., Kumar, A., Arnold, W., & Samwer, K. (2016). Elastic stiffness and damping measurements in titanium alloys using atomic force acoustic microscopy. *Journal of Alloys and Compounds*, *676*, 397–406. https://doi.org/10.1016/j.jallcom.2016.03.155

Rabe, U. (2006). Atomic force acoustic microscopy. In: Bhushan B., Fuchs H. (Eds), *Applied Scanning Probe Methods II* (pp. 37–90). Springer, Berlin, Heidelberg.

Reynolds, R. (1980). Interstratified clay minerals. In: Brindley, G.W., Brown, G. (Eds), *Crystal structures of clay minerals and their X-ray identification.* (pp. 249–303). Mineralogical Society, London.

Sader, J. E., Larson, I., Mulvaney, P., & White, L. R. (1995). Method for the calibration of atomic force microscope cantilevers. *Review of Scientific Instruments*, *66*(7), 3789–3798.

Santos, H., Diek, A., Da Fontoura, S., & Roegiers, J. (1997). Shale Reactivity test: A novel approach to evaluate shale-fluid interaction. *International Journal of Rock Mechanics and Mining Sciences*, *34*(3–4), 268–e1.

Shaoul, J. R., van Zelm, L. F., & De Pater, C. (2011). Damage Mechanisms in Unconventional-as-Well Stimulation—A New Look at an Old Problem. *SPE Production & Operations*, *26*(04), 388–400.

Sone, H., & Zoback, M. D. (2013). Mechanical properties of shale-gas reservoir rocks—Part 1: Static and dynamic elastic properties and anisotropy. *Geophysics*, *78*(5), D381–D392.

Stan, G., Ciobanu, C., Thayer, T., Wang, G., Creighton, J., Purushotham, K., et al. (2008). Elastic moduli of faceted aluminum nitride nanotubes measured by contact resonance atomic force microscopy. *Nanotechnology*, *20*(3), 035706.

Wang, F. P., & Reed, R. M. (2009). *Pore Networks and Fluid Flow in Gas Shales*. Paper presented at SPE Annual Technical Conference and Exhibition, New Orleans, Louisiana, USA. https://doi.org/10.2118/124253-MS

Wang, L., Bornert, M., Héripré, E., Chanchole, S., Pouya, A., & Halphen, B. (2015). Microscale insight into the influence of humidity on the mechanical behavior of mudstones. *Journal of Geophysical Research: Solid Earth*, *120*(5), 3173–3186. https://doi.org/10.1002/2015JB011953

Weaver Jr, W., Timoshenko, S. P., & Young, D. H. (1990). *Vibration problems in engineering*. Hoboken, NJ: John Wiley & Sons.

Wilkinson, T. M., Zargari, S., Prasad, M., & Packard, C. E. (2015). Optimizing nano-dynamic mechanical analysis for high-resolution, elastic modulus mapping in organic-rich shales. *Journal of Materials Science*, *50*(3), 1041–1049.

Wong, R., Schmitt, D., Collis, D., & Gautam, R. (2008). Inherent transversely isotropic elastic parameters of over-consolidated shale measured by ultrasonic waves and their comparison with static and acoustic in situ log measurements. *Journal of Geophysics and Engineering*, *5*(1), 103–117.

Wu, B., & Tan, C. (2010). *Effect of shale bedding plane failure on wellbore stability-example from analyzing stuck-pipe wells*. Paper presented at 44th U.S. Rock Mechanics Symposium and 5th U.S.-Canada Rock Mechanics Symposium, Salt Lake City, Utah, USA.

Wu, T., Zhao, J., Zhang, W., & Zhang, D. (2020). Nanopore structure and nanomechanical properties of organic-rich terrestrial shale: An insight into technical issues for hydrocarbon production. *Nano Energy*, *69*, 104426. https://doi.org/10.1016/j.nanoen.2019.104426

Yang, J., Hatcherian, J., Hackley, P. C., & Pomerantz, A. E. (2017). Nanoscale geochemical and geomechanical characterization of organic matter in shale. *Nature Communications*, *8*(1), 2179. https://doi.org/10.1038/s41467-017-02254-0

Yew, C. H., Wang, C. L., & Chenevert, M. E. (1992). *A theory on water activity between drill-fluid and shale*. Paper presented at 33th US Symposium on Rock Mechanics (USRMS), Santa Fe, New Mexico, USA.

Yuan, W., Li, X., Pan, Z., Connell, L. D., Li, S., & He, J. (2014). Experimental Investigation of Interactions between Water and a Lower Silurian Chinese Shale. *Energy & Fuels*, *28*(8), 4925–4933. https://doi.org/10.1021/ef500915k

Yuya, P. A., Hurley, D. C., & Turner, J. A. (2008). Contact-resonance atomic force microscopy for viscoelasticity. *Journal of Applied Physics*, *104*(7), 074916. https://doi.org/10.1063/1.2996259

Yuya, P., Hurley, D., & Turner, J. A. (2011). Relationship between Q-factor and sample damping for contact resonance atomic force microscope measurement of viscoelastic properties. *Journal of Applied Physics*, *109*(11), 113528.

Zeng, L., Wang, L., Xu, H., Jiao, G., Cui, S., Han, H., & Zhang, B. (2010). *SY/T 5163-2010. Analysis Method for Clay Minerals and Ordinary Non-clay Minerals in Sedimentary Rocks by the X-ray Diffraction*. Beijing, China: Petroleum Industry Publishing House.

Zhang, J., Zhu, D., & Hill, A. D. (2015). *Water-Induced Fracture Conductivity Damage in Shale Formations*. Paper presented at SPE Hydraulic Fracturing Technology Conference, The Woodlands, Texas, USA. https://doi.org/10.2118/173346-MS

Zhao, J., Zhang, D., Wu, T., Tang, H., Xuan, Q., Jiang, Z., & Dai, C. (2019). Multiscale Approach for Mechanical Characterization of Organic-Rich Shale and Its Application. *International Journal of Geomechanics*, *19*(1), 04018180. https://doi.org/10.1061/(ASCE)GM.1943-5622.0001281

List of Tables

Table 1. The mineral content of investigated samples (wt%).

Sample no.	Pyrite	Quartz	Feldspar	Clay	Carbonate	Others
Y12	3.9	9.8	12.4	62.0	2.8	9.1
Y13	1.3	8.9	10.7	68.6	7.5	3
Y21	2.1	8.5	11.8	67.2	9.0	1.4
YC1	1.5	16.3	2.86	76.8	/	2.54
YC2	2.9	14.9	4.57	71.3	1.1	5.23
YC3	1.1	12.7	1.73	84.1	/	0.37
YS109	2.9	32.4	16.2	33.6	14.9	/
YS111	/	49.2	19.7	31.1	/	/

Note: organic matter is not included.
Y - Triassic terrestrial shale; YC - Permian terrestrial shale; YS - Marine shale.

Table 2. The relative content of clay mineral based on clay enrichment (wt%).

Sample no.	Kaolinite	Chlorite	Illite	Smectite	I/S	C/S	Mixed ratio (%S)	
							I/S	C/S
Y12	1	2	5	/	92	/	5	/

Y13	10	8	6	/	76	/	7	/
Y21	4	6	16	/	74	/	5	/
YC1	65	/	10	/	25	/	5	/
YC2	37	13	21	/	29	/	5	/
YC3	89	/	1	/	10	/	5	/
YS109	/	/	41	/	59	/	5	/
YS111	/	/	43	/	57	/	5	/

Note: I/S: illite-smectite mixed-layer; C/S: chlorite-smectite mixed-layer.

Table 3. Comparison of measured elastic properties with published values. Contact resonance measured moduli are in good agreement with values reported in literatures.

Reference	**Elastic properties (GPa)**				**Test method**
	Pyrite	**Quartz**	**Clay**	**Organic matter**	
Mavko et al., 2009[Y]	250-312	77-96	1.5-25	2.5	-
Kumar et al., 2012[Y]	297±33	99±1	-	2-16	Quasi-static nanoindentation
Wilkinson et al., 2015[S]	>80	50-70	15-45	10	Dynamic nanoindentation
Eliyahu et al., 2015[Y]	-	63±8	29±1	0-25	Peak force QNM of AFM
Goodarzi et al., 2017[Y]	>100	78.5[a] 74.8[b]	32.5[a] 47.3[b]	6	Peak force QNM of AFM
Zhao et al., 2019[Y]	129.4	87.2	18.5[a] 29.4[b]	10.5	Dynamic nanoindentation and quasi-static nanoindentation
This work[S]	90-370	67.3[a] 69.2[b]	23.6[a] 37.6[b]	0-20	Contact resonance mapping of AFM

Note: [Y]Measured in Young's moduli; [S]Measured in storage moduli.

[a]Test region parallel to the bedding plane.

[b]Test region perpendicular to the bedding plane.

Figure Captions

Figure 1. Clay enrichment XRD results of terrestrial shale (YC2) and marine shale (YS109).

Figure 2. (a) Schematic diagram of an AFM contact resonance mode; (b) relationship between sample stiffness, dissipation, and resonance spectra, respectively.

Figure 3. (a) ESEM chamber with a cold stage below the test sample; (b) reduction of pressure required for experiments based on temperature control.

Figure 4. Comparison of electron image (BSE) and EDS elemental mapping for one test region of Y21a (test face parallel to the bedding plane).

Figure 5. Experimental procedure for mechanical characterization based on contact resonance of one region of Y21a: (a) topographic image obtained by scanning; (b) contact frequencies of different minerals; (c) contact frequency distribution from CR mapping; (d) storage modulus distribution from CR mapping.

Figure 6. Mechanical characterization for different minerals based on image threshold segmentation of one test region of Y21b (test face perpendicular to the bedding plane) from CR mapping: (a) SEM image of test region; (b) storage modulus distribution of organic matter; (c) storage modulus distribution of clay minerals; (d) storage modulus distribution of quartz and feldspar; (e) storage modulus distribution of pyrite; (f) storage modulus distribution of the entire test region.

Figure 7. Probability density functions and Gaussian mixture models of different constituents of one test region of Y21b.

Figure 8. Example region of mechanical variations before and after sample water imbibition: (a) SEM image of test area; (b) storage modulus mapping of test region before and after water imbibition, and relative changes of different minerals; (c) stiffness mapping of test region before and after water imbibition, and relative changes of different minerals; (d) viscoelastic properties mapping of test region before and after water imbibition, and relative changes of different minerals.

Figure 9. Mechanical characterization of the impact of water imbibition: (a) sample of terrestrial shale with test face parallel to the bedding plane; (b) sample of terrestrial shale with test face perpendicular to the bedding plane; (c) sample of marine shale with test face parallel to the bedding plane; (d) sample of marine shale with test face perpendicular to the bedding plane.

Figure 10. Statistical results of the influence of water sensitivity on the storage modulus variations of (a) terrestrial shale and marine shale with consideration of bedding plane orientation; (b) clay minerals and brittle minerals with consideration of bedding plane orientation.

Figure 11. Observation of hydration and dehydration process of a natural block sample at microscale.

Figure 12. Hydrophilicity differences of different minerals at microscale.

Figure 13. Observation of hydration and dehydration process of a clay cluster at nanoscale. The water film between clay particles appeared, and its radius curvature changed from R_1 to R_3 during the whole process, with R_2>R_1>R_3.

Figure 14. Observation of closing of void space or crack channels due to clay anisotropic swelling.

Figure 15. (a) (b) Observation of generation and propagation of micro-cracks due to dehydration-caused shrinkage; (c) the swelling of clay might also compress the surrounding minerals, thus increasing the modulus values of some measured minerals with increasing confining pressure (confining effect).

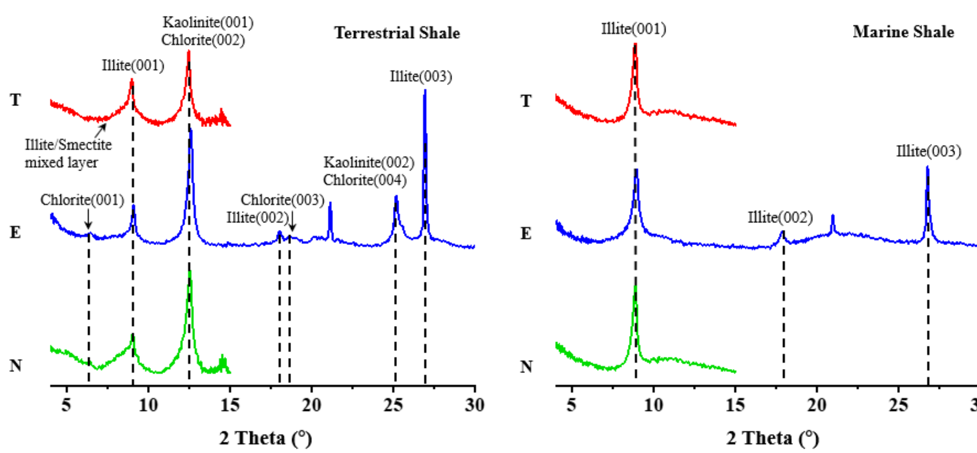

Note: N - natural state; E - ethylene glycol saturated state; T - heated state

Figure 1. Clay enrichment XRD results of terrestrial shale (YC2) and marine shale (YS109).

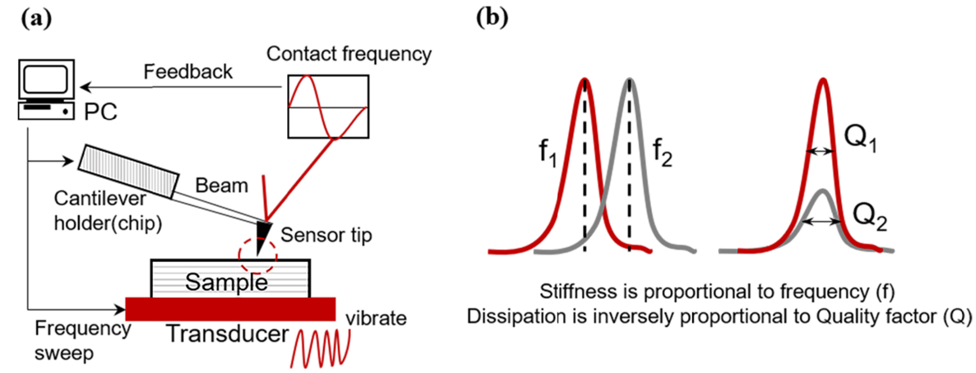

Figure 2. (a) Schematic diagram of an AFM contact resonance mode; (b) relationship between sample stiffness, dissipation, and resonance spectra, respectively.

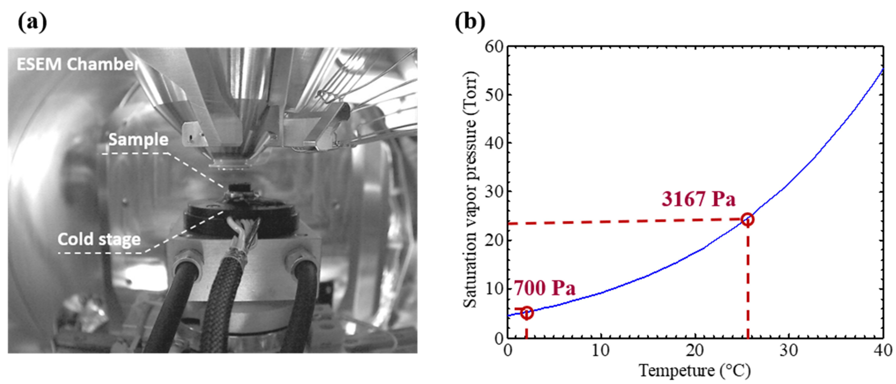

Figure 3. (a) ESEM chamber with a cold stage below the test sample; (b) reduction of pressure required for experiments based on temperature control.

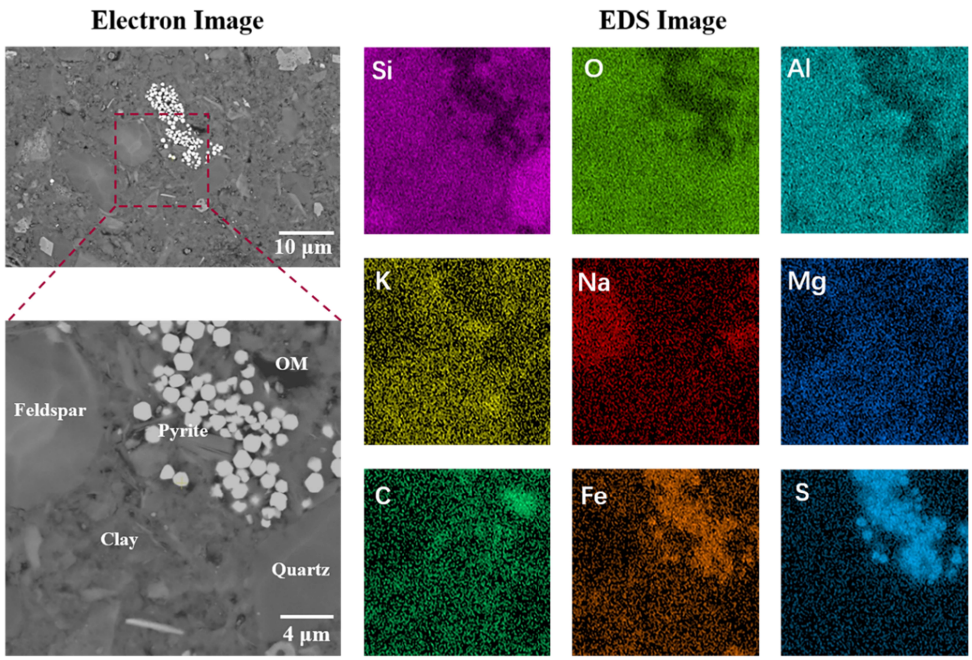

Figure 4. Comparison of electron image (BSE) and EDS elemental mapping for one test region of Y21a (test face parallel to the bedding plane).

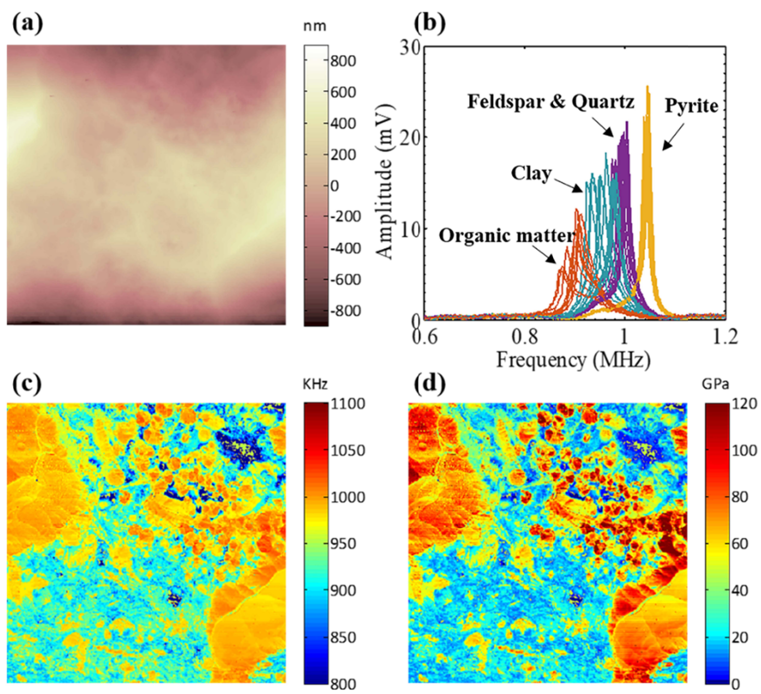

Figure 5. Experimental procedure for mechanical characterization based on contact resonance of one region of Y21a: (a) topographic image obtained by scanning; (b) contact frequencies of different minerals; (c) contact frequency distribution from CR mapping; (d) storage modulus distribution from CR mapping.

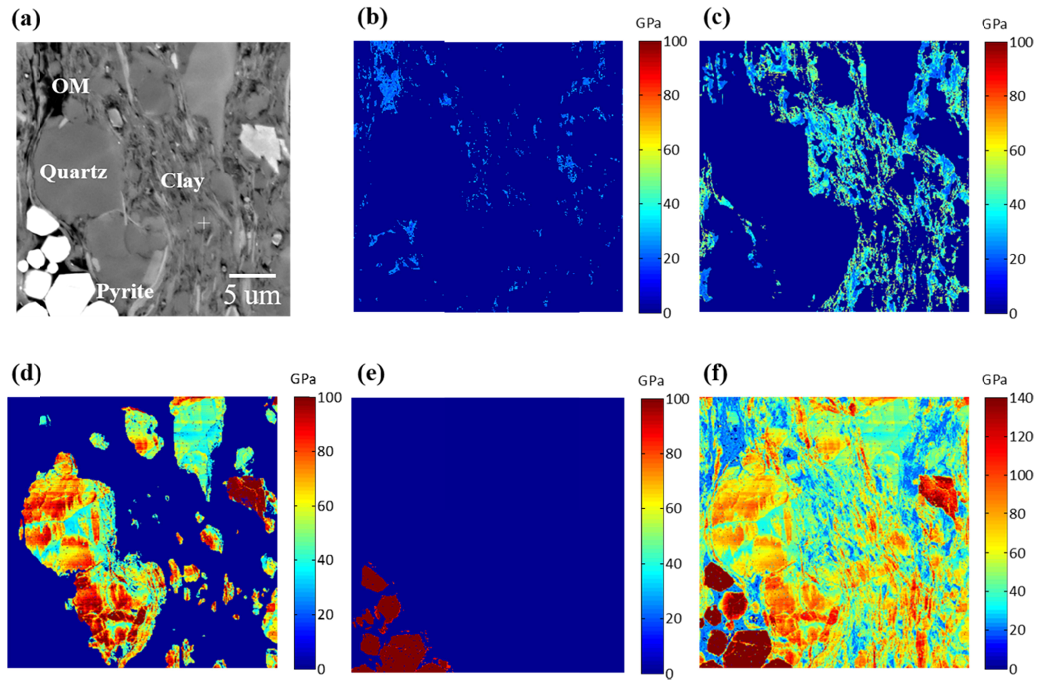

Figure 6. Mechanical characterization for different minerals based on image threshold segmentation of one test region of Y21b (test face perpendicular to the bedding plane) from CR mapping: (a) SEM image of test region; (b) storage modulus distribution of organic matter; (c) storage modulus distribution of clay minerals; (d) storage modulus distribution of quartz and feldspar; (e) storage modulus distribution of pyrite; (f) storage modulus distribution of the entire test region.

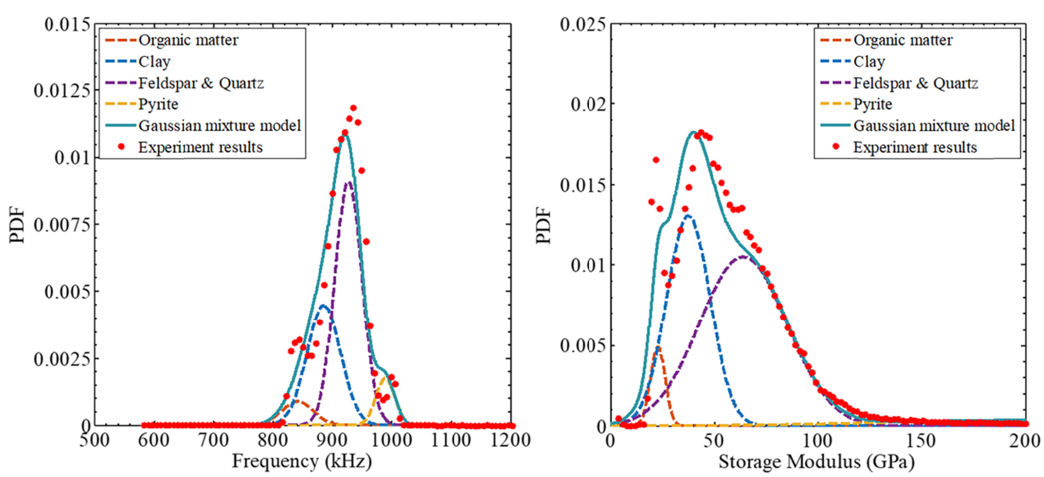

Figure 7. Probability density functions and Gaussian mixture models of different constituents of one test region of Y21b.

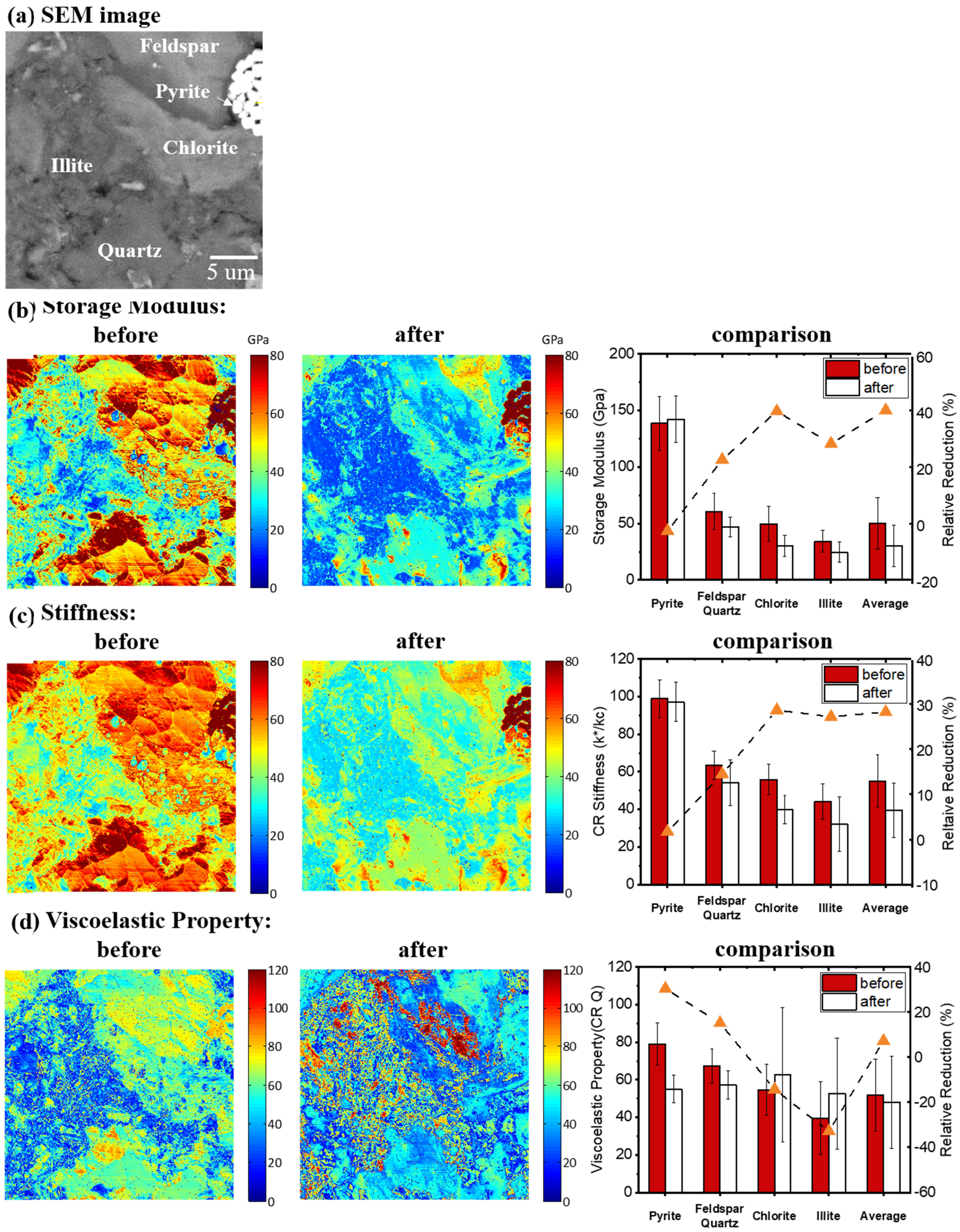

Figure 8. Example region of mechanical variations before and after sample water imbibition: (a) SEM image of test area; (b) storage modulus mapping of test region before and after water imbibition, and relative changes of different minerals; (c) stiffness mapping of test region before and after water imbibition, and relative changes of different minerals; (d) viscoelastic properties mapping of test region before and after water imbibition, and relative changes of different minerals.

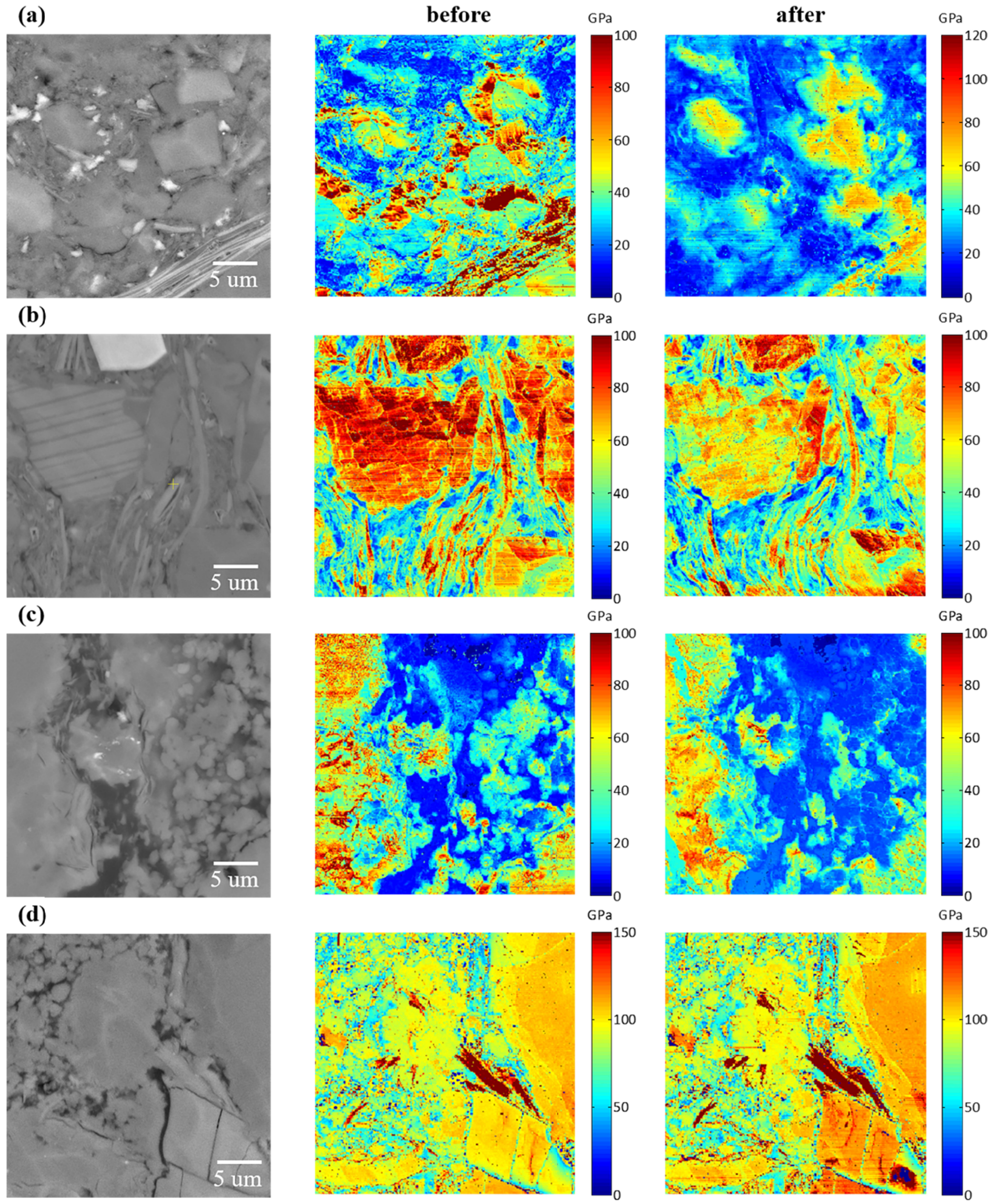

Figure 9. Mechanical characterization of the impact of water imbibition: (a) sample of terrestrial shale with test face parallel to the bedding plane; (b) sample of terrestrial shale with test face perpendicular to the bedding plane; (c) sample of marine shale with test face parallel to the bedding plane; (d) sample of marine shale with test face perpendicular to the bedding plane.

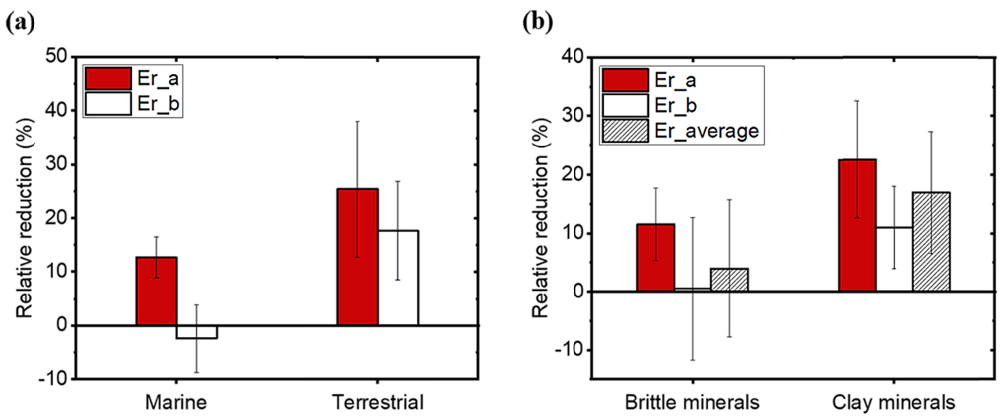

Note:
Er_a - measured modulus reduction perpendicular to the bedding direction;
Er_b - measured modulus reduction parallel to the bedding direction;
Er_average - measured average modulus reduction considering different bedding directions;
Brittle minerals: includes pyrite, quartz and feldspar etc.

Figure 10. Statistical results of the influence of water sensitivity on the storage modulus variations of (a) terrestrial shale and marine shale with consideration of bedding plane orientation; (b) clay minerals and brittle minerals with consideration of bedding plane orientation.

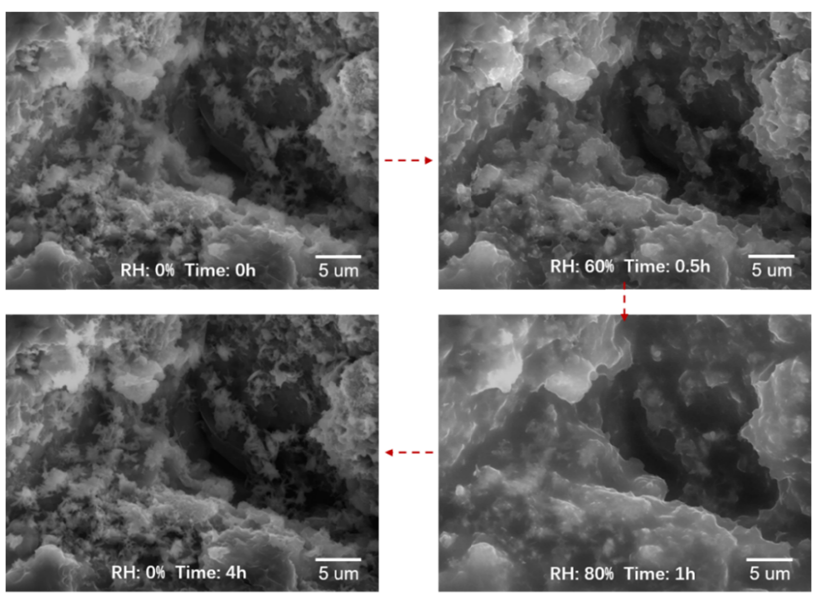

Figure 11. Observation of hydration and dehydration process of a natural block sample at microscale.

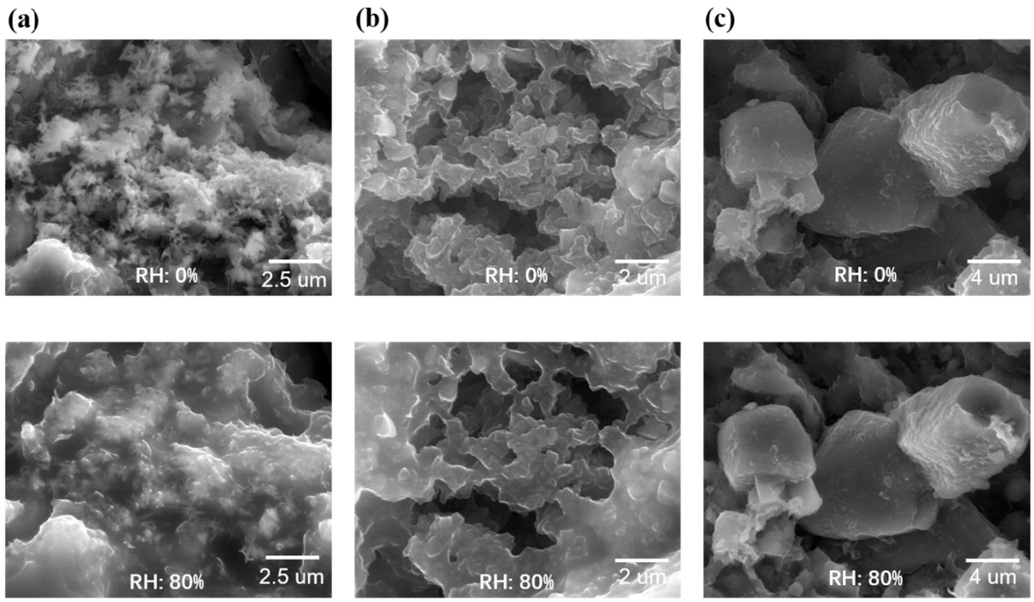

Figure 12. Hydrophilicity differences of different minerals at microscale.

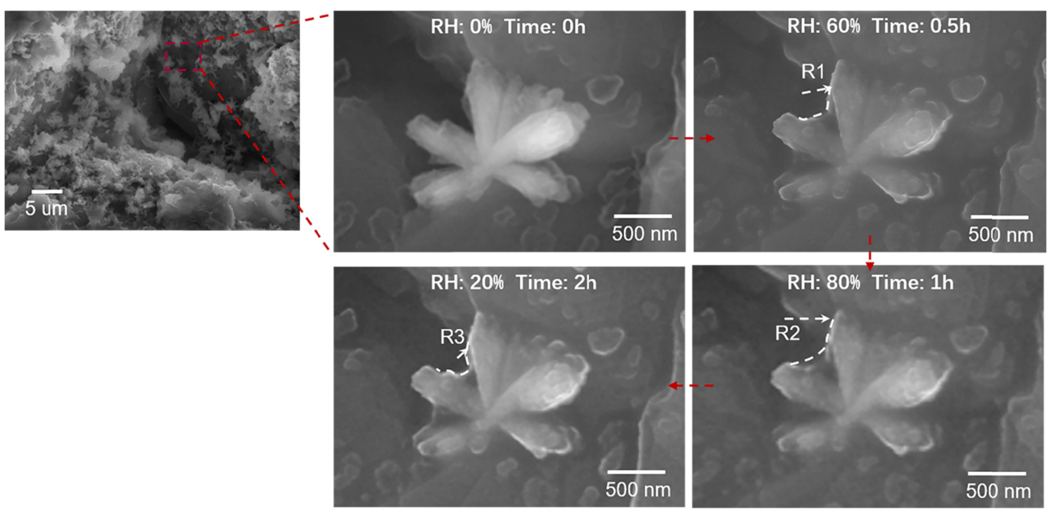

Figure 13. Observation of hydration and dehydration process of a clay cluster at nanoscale. The water film between clay particles appeared, and its radius curvature changed from R_1 to R_3 during the whole process, with R_2>R_1>R_3.

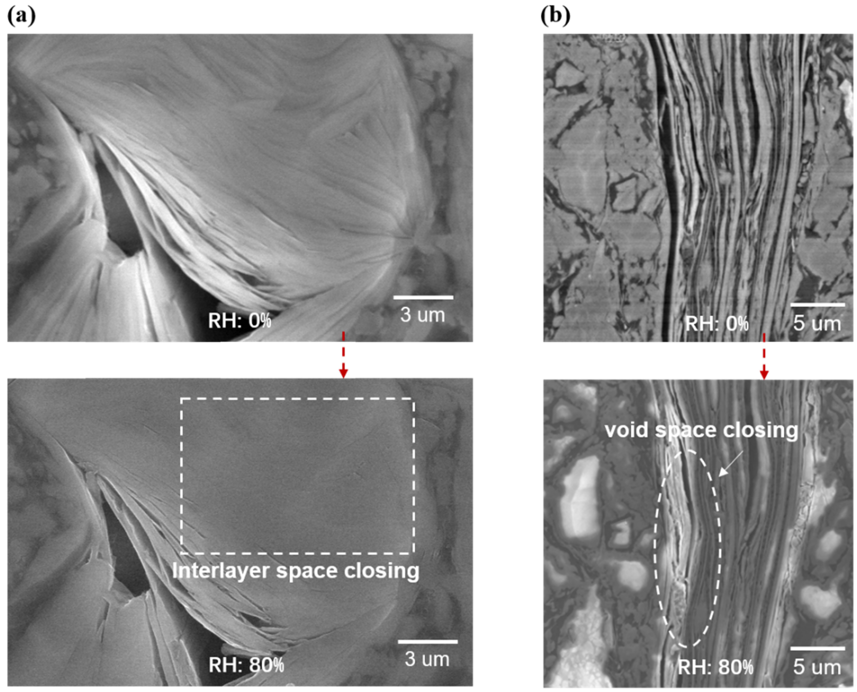

Figure 14. Observation of closing of void space or crack channels due to clay anisotropic swelling.

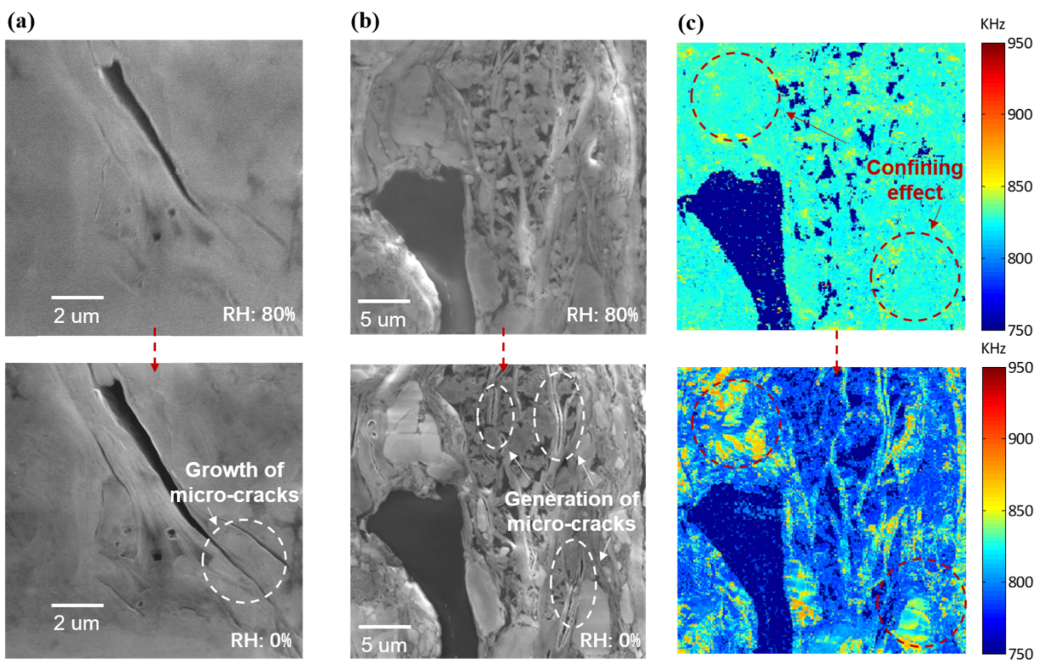

Figure 15. (a) (b) Observation of generation and propagation of micro-cracks due to dehydration-caused shrinkage; (c) the swelling of clay might also compress the surrounding minerals, thus increasing the modulus values of some measured minerals with increasing confining pressure (confining effect).